J. Phys. Chem. A **2003,** *107,* 621−631

Nonadiabatic Dynamics: A Comparison of Surface Hopping Direct Dynamics with Quantum Wavepacket Calculations

Graham A. Worth,* Patricia Hunt,[†] and Michael A. Robb

Department of Chemistry, King's College London, The Strand, London WC2R 2LS, U.K.

Received: October 2, 2002; In Final Form: November 20, 2002

A semiclassical direct dynamics method for nonadiabatic systems is tested by comparing with quantum wave packet dynamics, looking at the molecular dynamics of the butatriene molecule after formation of the radical cation in the first excited, $\tilde{A}$, state. There is a conical intersection coupling this state to the cationic ground state, $\tilde{X}$, and this plays a major role in the system evolution. The direct dynamics study consists of 80 trajectories, with the potential energy surfaces calculated on-the-fly using a complete active space (CASSCF) electronic wave function. The quantum dynamics used a model Hamiltonian and the multiconfigurational time-dependent Hartree (MCTDH) method to solve the time evolution of the nuclear wave packet. The results show that the methods give a similar description of the initial part of the dynamics, with a similar time scale for the interstate crossing. A qualitatively different behavior is, however, seen after crossing to the lower adiabatic surface, with a recurrence in the quantum dynamics not present in the direct dynamics. The direct dynamics also indicates the possible importance of a second intersection seam, which is not present in the model used for the quantum dynamics.

1. Introduction

The presence of a conical intersection between two electronic states can have a profound effect on the time evolution of a molecular system. This is particularly true after photoexcitation to the upper state: if the intersection is reached, nonradiative decay to the lower state occurs on an ultrafast, femtosecond, time scale. An understanding of the dynamics of such a process is crucial for an understanding of the mechanism of the reaction and the products formed, as relaxation to the lower state takes place in a coherent manner. Not only the topology of the conical intersection but also the initial conditions provided by the experimental preparation of the system and the path taken to the intersection play a role in the final outcome. Here, molecular dynamics simulations play a significant role in the description and visualization of these nonadiabatic processes.

A computer simulation of molecular dynamics (MD) needs two ingredients: a potential energy surface and an efficient way to propagate the system from the initial conditions over the surface. In this study we shall focus on the evaluation of the potential energy surface. Traditional dynamics methods, whether the nuclei are treated classically or quantum mechanically, need the potential energy surface as an analytical expression. This requires the global evaluation and fitting of the potential energy throughout coordinate space, a long and tedious process even for small molecules. For more than a few degrees of freedom the accurate evaluation becomes a hopeless task, and models must be used.

An alternative is to calculate the surface as and when it is required during the dynamics. This “direct dynamics” approach[1] has much appeal due to the great flexibility it would offer in the study of molecular dynamics. For large systems it is also a must for reasons of efficiency as the space not visited during the dynamics is enormous, and calculating the potential energy surface in these unexplored regions is a prohibitive waste of effort.

One problem applying direct dynamics to nonadiabatic systems is that the quantum chemistry method used to calculate the potential energy surface must be of reasonable quality on an excited state. The second problem is the dynamics algorithm to be used, in particular the question is how to include the nonadiabatic coupling. Molecular systems are quantum mechanical in nature, and the dynamics are described by the time-dependent Schrödinger equation. The nuclei should thus be described by a delocalized wave packet evolving in time. Calculating the potential on-the-fly, however, means that the potential energy surface is only known locally. As a result we turn to semiclassical methods, which use a description based on trajectories in a phase space. In a recent article[2] we review the field of direct dynamics, discussing both these points.

The question to be addressed in this paper is how good is a simple direct dynamics method for the description of a nonadiabatic process? The most popular method for the semiclassical dynamics of nonadiabatic systems is the trajectory surface hopping method.[3] In this, trajectories run over the upper surface until a region with strong nonadiabatic coupling is reached. Here the trajectories hop to the lower surface with a probability related to the strength of the coupling, so simulating the interstate crossing. An alternative method, which has already been used in direct dynamics studies, is the spawning method.[4,5] This in principle treats the nuclei in a fully quantum mechanical manner but is computationally more demanding.

A direct dynamics algorithm using surface hopping has already been implemented and applied to a number of systems, both using full complete active-space self-consistent field (CASSCF) wave functions[6,7] and the molecular mechanics-valence bond (MMVB) method, which simulates a CASSCF method.[8−12]

In these calculations, particularly using a full CASSCF wave function, it was not possible to run more than a few trajectories.

[†] Present address: Theoretical Chemistry, University of Cambridge, Cambridge, U.K.

10.1021/jp027117p CCC: $25.00

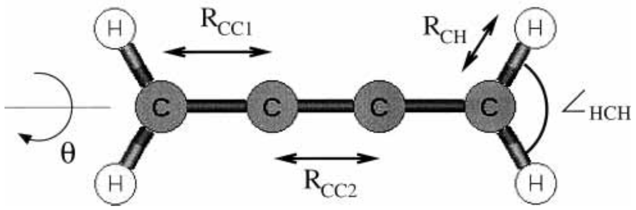

Figure 1. Geometrical parameters defining the structure of the butatriene molecule.

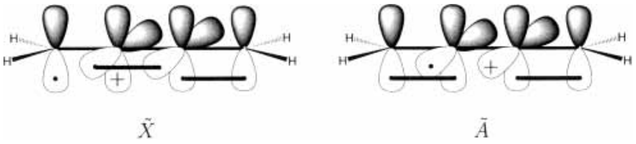

Figure 2. Orbitals involved in the coupled $\tilde{X}^2B_{2g}/\tilde{A}^2B_{2u}$ states of the butatriene radical cation. The active space used is effectively the six p-orbitals on the carbon atoms orthogonal to the carbon axis. A hole is denoted by a +, and an unpaired electron by a ●. − shows a bond. The $\tilde{X}^2B_{2g}$ has had an electron removed from the orbitals in the plane perpendicular to the molecular plane, whereas the $\tilde{A}^2B_{2u}$ state is formed by removing an electron from the orbitals in the molecular plane.

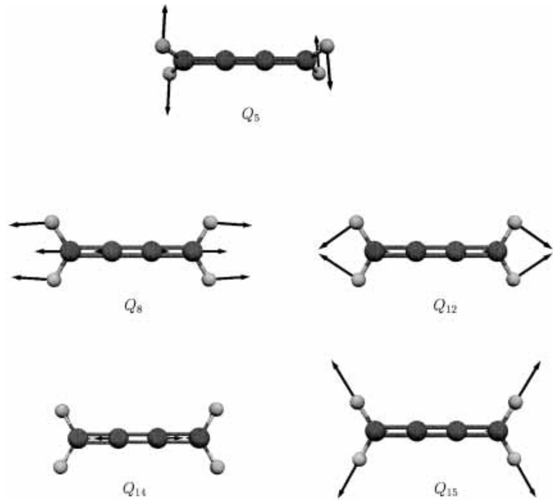

Figure 3. Important vibrational modes involved in the dynamics of the butatriene radical cation in the coupled $\tilde{X}^2B_{2g}/\tilde{A}^2B_{2u}$ electronic states, defined by the neutral ground-state normal modes calculated at the equilibrium D_{2h} geometry. Q_5 is the coupling mode with A_u symmetry and is related to the torsional motion. The remaining four modes are totally symmetric vibrations. Of particular importance is Q_{14}, the symmetric vibration of the central C−C bond.

Although the calculations were able to provide dynamical information to enhance understanding of the chemistry taking place, for accurate dynamics using surface hopping a large number of trajectories should be run. In this work we aim to test our trajectory surface hopping direct dynamics scheme by running a reasonable number of trajectories and comparing the results to full quantum molecular dynamics calculations. As a test case we take the formation of a butatriene radical cation in the $\tilde{A}^2B_{2u}$ state. In the photoelectron spectrum, the band arising from this state is linked to that from the $\tilde{X}^2B_{2g}$ state by a structured spectrum,[13] which is known to be due to a conical intersection between them.[14] As a test system it is ideal. It is a small organic molecule with a fairly simple electronic structure, and the quantum chemistry should be reasonable with a small basis set. The conical intersection also lies very close to, and is directly accessible from, the Franck−Condon region so that only short simulations are required to describe the nonadiabatic effects. As a prototypical conical intersection, it is also a good test of the method with physical relevance.

Shown in Figure 1, butatriene (C_4H_4) is a linear planar molecule with D_{2h} symmetry at the neutral ground-state equilibrium geometry. Figure 2 sketches the orbitals and Figure 3 the important nuclear modes for the system to be studied. In butatriene, three π-orbitals lie perpendicular to the carbon axis, and formation of the $\tilde{X}^2B_{2g}$ and $\tilde{A}^2B_{2u}$ states of the radical cation results from removal of an electron of the highest two occupied orbitals. These lie at right angles to one another, with the $\tilde{X}$ state being formed by making a hole in a molecular orbital that lies above and below the plane of the molecule and the $\tilde{A}$ state hole being in a molecular orbital that lies in the plane. Torsional motion around the axis leads to vibronic coupling between these states. The central C−C symmetric stretch vibration also plays a major role in the vibronic coupling, providing the second degree of freedom required for the formation of a conical intersection between the states.

The quantum dynamics were made using a vibronic coupling model Hamiltonian[15] for the coupled $\tilde{X}/\tilde{A}$ states in the butatriene radical cation. This model has been successfully applied to a number of problems in which the system passes through a conical intersection within a few femtoseconds after excitation. In a recent paper, Cattarius et al.[16] set up a model Hamiltonian for the coupled states, treating five nuclear degrees of freedom explicitly. This model, which is complete to first order in the coupling, reproduces the spectrum for this system very well, and hence describes the major features of the molecular dynamics. Here, to use it as a comparison for the direct dynamics calculations, we reparametrize this Hamiltonian to reproduce the CASSCF potential energy surfaces.

2. Theory and Methods

2.1. Electronic Structure and Direct Dynamics Calculations. The direct dynamics and quantum chemistry calculations were made using a development version of the GAUSSIAN program.[17] The potential energy, gradient, and force constants for the butatriene radical cation ground and first excited states were evaluated using a CASSCF method. The active space chosen was to distribute the π-electrons (six for calculations on the neutral species and five for the radical cation) in the six π-orbitals. As can be shown by localization,[18] the active space used can be thought of as comprising the six carbon p-orbitals that do not contribute to the σ-bonding framework. Each carbon contributes a p-orbital perpendicular to the molecular plane, while the central two carbon atoms also provide two p-orbitals that lie in the plane. The active space used is sketched in Figure 2. The calculations are labeled CAS(N,M)/X, where N is the number of electrons and M the number of orbitals in the active space, and X denotes the basis set used. In all the results presented here, a basis set of 3-21G* was used. As we are comparing theory with theory, the basis set used is not critical. That it at least provides a reasonable description of the butatriene molecule was shown by comparison with 6-31G* calculations at a number of geometries, which showed no major differences.

For the semiclassical trajectory calculations, a set of points in phase space must first be generated to represent the nuclear wave packet. This was done by sampling the neutral ground-state using the normal-mode sampling algorithm.[19,20] Half a quantum of energy was put into each normal mode and a set of positions and momentum set up by random sampling, with a correction made to scale the initial harmonic guess to the true potential surfaces. In this way the zero point energy of the ground-state system is approximately included. A more faithful representation of the quantum wave packet would be to sample a Wigner, or similar, distribution that maps the quantum wave packet onto phase space.[21] This would, however, mean that even more trajectories would be required, and experience seems to show that the classical distribution taken here is reasonable.

The wave packet was then propagated using a trajectory surface hopping method. Starting on the upper adiabatic surface, each point evolves along a classical trajectory. The integration scheme for the trajectories was the Helgaker−Chen algorithm.[1,22] This uses a harmonic approximation to the surface to generate a predictor step, followed by a corrector step using a fifth-order polynomial fit to the true surface. Despite the need for calculating the Hessian matrix and its eigenvalues at each step, this method is efficient due to the very large steps that can be taken.

The probability of hopping between surfaces was obtained from the state populations calculated by propagating the electronic wave function. Using the basis of state functions, $\{\psi_i\}$, the electronic wave function can be represented by the vector of coefficients, $\mathbf{a}(t)$. This vector can then be propagated in time by solving

$$\mathbf{a}(t+\tau) = \exp(-\mathrm{i}\mathbf{H}\tau)\mathbf{a}(t) \tag{1}$$

where $\mathbf{H}$ is the electronic Hamiltonian in the state function basis. The squares of the vector elements give the population of the electronic states as a function of time (see ref 23 for more details), and a hop between surfaces was performed if the probability for the populated state drops below 0.65.

Smaller steps are needed for the time evolution of the electronic wave function than are required for the integration of the nuclear equations of motion. For this reason, and as the probability of hopping is negligible until the surfaces become close, the electronic wave function propagation is only started when the energy gap between the states goes below a limit of 0.04 hartree. It is then stopped when the gap goes back above this value. To save computational effort, the Hessian matrix is updated rather than recalculated at each step during this time. As is usual in surface hopping methods, the energy is conserved after a hop by correcting the momentum in the direction of the derivative coupling vector $\mathbf{F}_{ij} = \langle\psi_i|\nabla\psi_j\rangle$.[24] After a hop takes place, a wait of 5 fs is made to allow the system to adjust to the new surface before testing for a hop again.

When the surfaces are close in energy, state-averaged orbitals have to be used to ensure convergence of the CASSCF wave function. When this is not the case, however, non-state-averaged orbitals should be used. To make a smooth transition between the two regimes, the weighting factor for the averaging was changed over a number of steps. Assuming that the system is initially in state 2 outside the nonadiabatic region, the weights (0.0, 1.0) are used. Once a gap of 0.05 hartree is reached, the weights were changed by 0.1 over 5 steps until fully state-averaged orbitals weighted (0.5, 0.5) were used. After moving back out of the nonadiabatic region the weights were again smoothly reversed so that the wave function for a single state was optimized.

2.2. Vibronic Coupling Model Hamiltonian. To describe a nonadiabatic system, we start by assuming a diabatic representation; i.e., the Hamiltonian is written in matrix form as

$$\mathbf{H}(\mathbf{Q}) = \hat{T}_{\mathrm{N}}\mathbf{1} + \mathbf{W}(\mathbf{Q}) \tag{2}$$

where $\hat{T}_{\mathrm{N}}$ is the nuclear kinetic energy operator and $\mathbf{1}$ is the unit matrix. Matrix elements refer to the electronic states accessible to the system, and coupling between electronic states is provided by off-diagonal elements in the potential operator matrix, $\mathbf{W}$. This contrasts to the adiabatic representation in which

$$\mathbf{H}(\mathbf{Q}) = \hat{T}_{\mathrm{N}}\mathbf{1} - \Lambda(\mathbf{Q}) + \mathbf{V}(\mathbf{Q}) \tag{3}$$

where the diagonal matrix $\mathbf{V}(\mathbf{Q})$ contains the solutions to the clamped nucleus electronic Hamiltonian at nuclear coordinate $\mathbf{Q}$, and Λ is the nonadiabatic coupling operator, a nonlocal operator responsible for coupling motion on the different adiabatic potential energy surface. The two representations are connected by a transformation that diagonalizes the potential matrix at every point in space

$$\mathbf{V}(\mathbf{Q}) = \mathbf{S}(\mathbf{Q})^{\dagger}\,\mathbf{W}(\mathbf{Q})\,\mathbf{S}(\mathbf{Q}) \tag{4}$$

Thus the diabatic representation assumes that the transformation is such that the nonlocal nonadiabatic operator is transformed into the local diabatic potential matrix. For more details see, e.g., refs 2 and 15.

The vibronic coupling model expresses the potential matrix $\mathbf{W}$ by Taylor expansions about a suitable point, $\mathbf{Q}_0$, and zeroth-order potential, $W_i^{(0)}$

$$W_{ij} - W_i^{(0)}\delta_{ij} = \langle\phi_i|H_{\mathrm{el}}|\phi_j\rangle + \sum_{\alpha=1}^{f}\left[\frac{\partial}{\partial Q_\alpha}\langle\phi_i|H_{\mathrm{el}}|\phi_j\rangle\right]Q_\alpha + \ldots \tag{5}$$

where H_{el} is the usual clamped nucleus electronic Hamiltonian, ϕ_i is the diabatic electronic wave functions, and the integrals and derivatives are evaluated at the point $\mathbf{Q}_0$. The arbitrary phase of the diabatic functions is taken care of by setting them equal to the adiabatic functions at $\mathbf{Q}_0$. As a result,

$$W_{ii} = E_i + W_i^{(0)} + \sum_{\alpha=1}^{f}\kappa_\alpha^{(i)}Q_\alpha + \ldots \tag{6}$$

$$W_{ij} = \sum_{\alpha=1}^{f}\lambda_\alpha^{(ij)}Q_\alpha + \ldots \tag{7}$$

where $E_i = V_i(\mathbf{Q}_0)$ is the adiabatic energy at $\mathbf{Q}_0$, and κ and λ are the expansion coefficients defined in eq 5.

The situation to be described is an excitation from the neutral ground state into the coupled manifold of radical cation states. For this reason, $\mathbf{Q}_0$ is taken as the neutral ground-state equilibrium geometry, which is the Franck−Condon point on excitation, and $W_i^{(0)}$ for both states is the neutral ground-state potential energy surface. Taking the latter in a harmonic approximation, the natural coordinates for the system are then the neutral ground-state normal modes, i.e., the eigenfunctions of the Hessian (potential second-derivative) matrix at $\mathbf{Q}_0$. Scaling these so they become dimensionless (mass-frequency weighted) coordinates, the zero-order potentials are

$$W^{(0)} = \sum_\alpha \frac{\omega_\alpha}{2}{Q_\alpha}^2 \tag{8}$$

and the kinetic energy operator is

$$\hat{T}_{\mathrm{N}} = \sum_\alpha -\frac{\omega_\alpha}{2}\frac{\partial^2}{\partial {Q_\alpha}^2} \tag{9}$$

Note that atomic units have been implicitly used with $\hbar = 1$.

A huge simplification is now obtained by considering the symmetry of the coordinates and electronic states. The integrals for the coupling constants κ and λ are only nonzero if the symmetry product of the electronic wave functions ϕ_i and ϕ_j and the nuclear coordinate, Q_α, contain the totally symmetric irreducible representation:

$$\Gamma_i \otimes \Gamma_\alpha \otimes \Gamma_j \supset A_g \tag{10}$$

Thus to first order (linear vibronic coupling) only totally symmetric coordinates appear on the diagonal, and only modes of a particular symmetry appear on the off-diagonal.

In the butatriene radical cation, at the neutral ground-state equilibrium geometry the electronic states of interest are $\tilde{X}^2B_{2g}$ and $\tilde{A}^2B_{2u}$. Given that the point group at this geometry is D_{2h}, the model complete to first order includes five degrees of freedom. These are the four totally symmetric vibrational modes, ν_8, ν_{12}, ν_{14}, and ν_{15}, which provide the on-diagonal terms, and the one vibrational mode with A_u symmetry, ν_5, which provides the off-diagonal coupling. All other nuclear coordinates couple only to second order with bilinear and quadratic terms, which have been shown to be small in butatriene.[16] Neglecting these higher order terms, the potential energy surface for these 13 modes is simply the zero-order Hamiltonian, the sum of the neutral ground-state harmonic functions. On excitation, these modes are thus not excited and play no role in the initial molecular dynamics. In general, it is found that these weak second-order terms play a role at longer times, typically after a few hundred femtoseconds, by providing a bath into which the energy slowly flows, causing the wave packet to spread out and dephase.

A more realistic model for the dynamics is obtained if the coupling mode is taken as the dihedral angle, θ. The transformation from the normal mode coordinate to the torsion angle is

$$Q_5 \rightarrow r_0\sqrt{\omega_5 m_H}\,\theta \tag{11}$$

where r_0 is the distance from the hydrogen atom, which has mass m_H, to the carbon−carbon axis, and ω_5 is the frequency of the neutral ground-state normal vibration. The kinetic energy operator for this degree of freedom in eq 9 is then transformed

$$-\frac{\omega_5}{2}\frac{\partial^2}{\partial Q_5{}^2} \rightarrow -\frac{1}{2I}\frac{\partial^2}{\partial\theta^2} \tag{12}$$

where the moment of inertia around the torsion angle is $I = 2m_H r_0{}^2$. The zero-order potential in eq 8 is also replaced by the trigonometric series

$$\frac{\omega_5}{2}Q_5{}^2 \rightarrow \sum_n A_n \sin^2(n\theta) \tag{13}$$

and the linear intrastate coupling by the term

$$\lambda_5 Q_5 \rightarrow \lambda_5 r_0\sqrt{\omega_5 m_H}\,\sin\theta \tag{14}$$

TABLE 1: Parameters Used in the Vibronic Coupling Model Hamiltonian[a]

mode	ω	$\kappa^{(1)}$	$\kappa^{(2)}$
$Q_8(1A_g)$	0.1117	−0.0456	−0.0393
$Q_{12}(2A_g)$	0.2021	0.0399	0.0463
$Q_{14}(3A_g)$	0.2723	−0.2139	0.2877
$Q_{15}(4A_g)$	0.4102	−0.0864	−0.1352
$\theta(A_u)$	A_n	$\lambda = 0.3289$	
$n = 1$	1.4823		
$n = 2$	−0.2191		
$n = 3$	0.0525		
$n = 4$	−0.0118		
$E_1 = 8.5037$		$E_2 = 9.4523$	

[a] The coordinates are the neutral ground-state totally symmetric normal modes and the torsion angle. See section 2.2 for details. For comparison with earlier work[16] values are in eV.

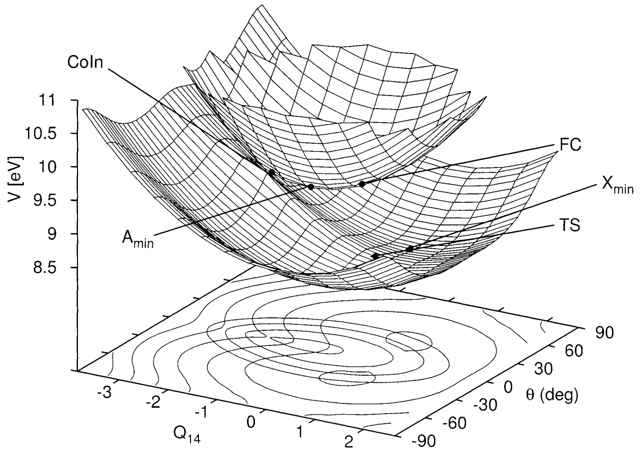

Figure 4. Potential energy surfaces for the $\tilde{X}^2B_{2g}/\tilde{A}^2B_{2u}$ states of the butatriene radical cation in the space of the symmetric stretch vibration, Q_{14}, and the torsional mode, θ, as given by the linear vibronic coupling model Hamiltonian. The upper cone belongs to the $\tilde{A}$, and the lower sheet the $\tilde{X}$ adiabatic electronic state. Critical points are marked: FC is the Franck−Condon point, CoIn the lowest energy point on the conical intersection seam, A_{min} and X_{min} the minima on the two surfaces, and TS the transition state point.

The parameters for this model evaluated previously[16] result in a spectrum in very good agreement with the experimental one. In particular, the intensity and structure between the expected bands due to the breakdown of the Born−Oppenheimer approximation is reproduced very well. The neglect of the other modes in this process is thus justified. In this work, the model potential energy surface must match as closely as possible the potentials used in the direct dynamics to allow a comparison of the two methods. The parameters were thus reevaluated by fitting to energies calculated at the CAS(5,6)/3-21G* level at a range of geometries. The root mean-square deviation (RMSD) between the model and quantum chemistry values was 0.06 eV over 106 points. These parameters are listed in Table 1.

2.3. Critical Points and Vectors. A dynamical process is dependent on the topology of the potential energy surface traversed, and its description can be made using critical points and vectors on the surface. The obvious coordinate system in which to work are the dynamical variables of the model Hamiltonian presented above. These are a reduced set of nuclear coordinates that can describe the major features of the nuclear dynamics in terms of the molecular motion, and comprise the torsional angle and the four symmetric neutral ground-state normal-mode coordinates. To define points (or other vectors) on the surfaces, we will use the vector with components

$$\mathbf{Q} = (\theta, Q_8, Q_{12}, Q_{14}, Q_{15}) \tag{15}$$

where Q_i are the dimensionless normal-mode coordinates introduced in the last section, associated with the vibration ν_i of the neutral species, and θ the torsion angle in degrees. These are shown in Figure 3. To connect to the molecule, results will also be given in terms of the geometrical parameters shown in Figure 1. The critical points are shown graphically in Figure 4.

The first point of interest is the Franck−Condon point, $\mathbf{Q}_{FC}$, the center of the initial wave packet. The vector of force away from this point, $\mathbf{F}_{FC}$, is the line of initial motion in a classical picture. The upper adiabatic surface is then characterized by the position and depth of the minima at $\mathbf{Q}_{\tilde{A}}$, and by the conical intersection seam through which the interstate crossing occurs. To characterize the conical intersection, we use the lowest energy point on the seam $\mathbf{Q}_{CoIn}$, and the gradient difference and derivative coupling vectors, $\mathbf{F}_{GD}$ and $\mathbf{F}_{DC}$, respectively. The energy difference between $\mathbf{Q}_{CoIn}$ and $\mathbf{Q}_{FC}$ dictates whether the intersection is energetically accessible to the excited system, whereas the two force vectors provide the "branching space" in which the degeneracy of the seam is lifted. After changing states, the wave packet will bifurcate in this space as it moves away from the conical intersection. Finally, the minima on the lower surface are the points at which the system could end if the energy is dissipated to the environment. They thus define the configurations accessible to the photoexcited molecule. In butatriene there are two minima, denoted $\mathbf{Q}_{\tilde{X}}$, which are equivalent due to symmetry. They are separated by a transition state at $\mathbf{Q}_{TS}$.

Before progressing, the vectors $\mathbf{F}_{GD}$ and $\mathbf{F}_{DC}$ will be defined. A conical intersection occurs when two potential energy surfaces become degenerate. At such a point it is easier to describe the system by expressing the Hamiltonian using a diabatic electronic basis, eq 2. The adiabatic surfaces are then given by

$$V_{\pm} = \frac{1}{2}(W_{11} + W_{22}) \pm \sqrt{\Delta W^2 + {W_{12}}^2} \tag{16}$$

where $\Delta W = 1/2(W_{22} - W_{11})$. We now move to a point of degeneracy, which occurs when

$$\Delta W = W_{12} = 0 \tag{17}$$

Here the diabatic wave functions are set equal to the adiabatic functions. Making a Taylor expansion of the diabatic matrix elements around this point, these terms can be written to first order in vector notation as

$$\Delta W = \mathbf{F}_{GD} \cdot \mathbf{Q} \tag{18}$$

$$W_{12} = \mathbf{F}_{DC} \cdot \mathbf{Q} \tag{19}$$

with the components of the vectors defined by

$$F^{\alpha}_{GD} = \frac{\partial}{\partial Q_{\alpha}} \Delta W \tag{20}$$

$$F^{\alpha}_{DC} = \frac{\partial}{\partial Q_{\alpha}} W_{12} \tag{21}$$

where the derivatives are evaluated at $\mathbf{Q}_{CoIn}$. Moving in the $n - 2$-dimensional space orthogonal to the vectors $\mathbf{F}_{GD}$ and $\mathbf{F}_{DC}$, the degeneracy of the states is retained as eq 17 holds, whereas moving in this space the degeneracy is lifted. From eq 16 it can be seen that in the branching space, the adiabatic potential energy surface has the form of a double cone, hence the name conical intersection.

All these points and vectors on both radical cation potential energy surfaces can be calculated using CASSCF methods. Transformation to the dynamical coordinates was made using the normal modes calculated at the neutral ground-state minimum at the CAS(6,6)/3-21G* level. The minima on both surfaces were located using standard energy optimization, whereas the lowest energy point on the conical intersection involves a constrained optimization to find the lowest energy point along the degenerate seam.[25,26] Finally, the transition structure on the lower cationic surface is found by optimization of the molecule in the planar, D_{2h}, symmetry. See ref 27 for further details of how to characterize a potential energy surface.

One of the advantages of the linear vibronic coupling model is that analytic expressions can be obtained for the critical points. The Franck−Condon point $\mathbf{Q}_{FC}$ is the point $\mathbf{Q}_0$, and the force $\mathbf{F}_{FC}$ is the vector of linear coupling coefficients, $(0, \kappa^{(2)}_{8}, \kappa^{(2)}_{12}, \kappa^{(2)}_{14}, \kappa^{(2)}_{15})$. The expression for the position of the lowest energy point on the conical intersection seam is more complicated but is given in section 3 of ref 15. Using the parameters from the model to define

$$\sigma_{\alpha} = \frac{1}{2}(\kappa^{(1)}_{\alpha} + \kappa^{(2)}_{\alpha}) \qquad \delta_{\alpha} = \frac{1}{2}(\kappa^{(2)}_{\alpha} - \kappa^{(1)}_{\alpha}) \tag{22}$$

and

$$D = \sum_{\alpha} \frac{{\delta_{\alpha}}^2}{\omega_{\alpha}} \qquad F = \sum_{\alpha} \frac{\delta_{\alpha}\sigma_{\alpha}}{\omega_{\alpha}} \qquad \Delta = \frac{1}{2}(E_2 - E_1) \tag{23}$$

the coordinates of the lowest energy point on the conical intersection are

$$Q_{CoIn,\alpha} = \frac{\delta_{\alpha}}{\omega_{\alpha}} \frac{F - \Delta}{D} - \frac{\sigma_{\alpha}}{\omega_{\alpha}} \tag{24}$$

Note that only the symmetric modes are changed, all other coordinates retain the value at the Franck−Condon point.

To find the gradient difference and derivative coupling vectors, the origin of the coordinate system can be shifted along the totally symmetric coordinates to $\mathbf{Q}_{CoIn}$. Here, the elements of the vectors are given by

$$\mathbf{F}^{\alpha}_{GD} = \delta'_{\alpha} = \frac{1}{2}({\kappa'_{\alpha}}^{(2)} - {\kappa'_{\alpha}}^{(1)}) \tag{25}$$

$$\mathbf{F}^{\alpha}_{DC} = \lambda_{\alpha} \tag{26}$$

where

$${\kappa'_{\alpha}}^{(i)} = \kappa^{(i)}_{\alpha} + \omega_{\alpha} Q_{CoIn,\alpha} \tag{27}$$

An analytic expression for the position of the transition state on the lower surface is also found by minimizing the energy of the lower adiabatic surface with $\theta = 0°$, i.e.

$$Q_{TS,\alpha} = -\frac{\kappa^{(1)}_{\alpha}}{\omega_{\alpha}} \tag{28}$$

where α again refers to one of the symmetric vibrational coordinates. Unfortunately, in contrast to the case when the coupling mode is treated using a harmonic oscillator, the Fourier series used for the torsional angle diabatic potential means that a simple analytic expression is not possible for the minima on the adiabatic surfaces. These were found by numerical optimization.

2.4. Wave Packet Propagation. The wave packet dynamics were carried out using the very efficient MCTDH method as implemented in the Heidelberg MCTDH package.[28−30,32] In this, the nuclear wave function is expanded in a time-dependent basis set

$$\psi(Q_1 \ldots Q_f, t) = \sum_{\alpha} \sum_{j_1 \ldots j_f} A^{(\alpha)}_{j_1 \ldots j_f}(t) \varphi^{(1,\alpha)}_{j_1}(Q_1, t) \ldots \varphi^{(f,\alpha)}_{j_f}(Q_f, t) \tag{29}$$

TABLE 2: Technical Details of the MCTDH Calculations[a]

particles	N	n
θ, Q_{14}	(41, 15)	[8, 8]
Q_{12}, Q_{15}	(10, 10)	[8, 8]
Q_8	(15)	[6, 6]

[a] The five modes were combined together into three particles for efficiency. N is the no. of primitive basis functions used for each degree of freedom. Harmonic oscillator DVR functions were used for the vibrations, Q_α, and an exponential DVR for the torsion angle, θ. n is the no. of single particle functions used for the wave function in the [$\tilde{\mathrm{X}}$, $\tilde{\mathrm{A}}$] diabatic states.

The index α refers to the electronic states of the system, and so a different basis set is used for each state. The indices j_1, j_2, ... label the basis functions. Both the expansion coefficients and the functions are then propagated by equations of motion derived from a variational solution of the time-dependent Schrödinger equation. As a result, the basis functions, known as single-particle functions, optimally describe the evolving wave packet at all times. For details of the equations of motion and how they are solved, see ref 30.

The single-particle functions are themselves described by one-dimensional time-independent basis sets using a discrete variable representation (DVR). For the normal modes in the vibronic coupling Hamiltonian, a harmonic oscillator DVR is used. For the torsional angle, an exponential DVR is used. This automatically introduces periodic boundary conditions for this degree of freedom. Details are given in the appendices of ref 30.

The single-particle functions need not be one-dimensional as indicated by eq 29, i.e., they describe more than one degree of freedom. By using this flexibility, the computational requirements can be significantly reduced. The computational requirements scale approximately with $p^2 n^{p+1} + pnN^2$, where p is the number of sets of single-particle functions, n is the number of functions, and N is the number of grid points used to describe the functions. Thus by combining degrees of freedom together, p is made smaller and the number of expansion coefficients n^p reduced. In doing this, however, the number of grid points, N, increases as the product primitive grids for the combined degrees of freedom are now required here. For best efficiency a balance must be found between reducing p and increasing N.

Numerical details of the MCTDH calculations are given in Table 2. Thus the degrees of freedom θ and Q_{14} are treated using a set of 2-dimensional single-particle functions, as are the Q_{12} and Q_{15} modes. The number of DVR grid points is then given for each degree of freedom, so for example, the (θ, Q_{14}) particle had a grid of $41 \times 15 = 615$ points. The number of single-particle functions for each set required for converged calculations starting in the upper, $\tilde{\mathrm{A}}$, state are also given for the wave packet in each state. The compact nature of the MCTDH method can be easily seen by the number of complex numbers required for the representation of the wave function. Using a standard wave packet method, which represents the nuclear wave function in the full product primitive basis, 922 500 numbers are required. The MCTDH wave function needs only 12 388 numbers.

The process under study is the ejection of an electron by the interaction of the molecule with light. Such a process is modeled by the transition from the neutral ground state to a diabatic excited state. Only then is the transition dipole moment relatively constant throughout the relevant space, which is necessary for the Condon approximation to be valid. The neutral ground-state wave function in the space of the five modes of the model is a product of harmonic oscillator (Gaussian) functions for the four symmetric modes, and the lowest eigenfunction from the ground-state torsional potential. This potential function is the Fourier series eq 13 with the coefficients given in Table 1. As the matrix elements of the Hamiltonian operator relate to the diabatic representation, the initial wave packet for the dynamics is formed simply by putting this wave function in the desired state by setting the coefficient for this configuration, $A^{(2)}_{111}$, to 1.0 and all the other coefficients to zero.

Many properties can be directly obtained from the time-dependent wave function, such as expectation values of coordinates. An exception is the adiabatic state populations required for the comparison with the direct dynamics surface hopping calculations, which requires that the wave packet is expressed in the adiabatic representation. For this the wave packet must be transformed using the matrixes $\mathbf{S}(\mathbf{Q})$ defined in eq 4. These are complicated multidimensional operators and can only be applied to the wave packet on the full product primitive grid. The wave packet was thus saved every 5 fs, and only these were transformed to the desired representation.

3. Results

3.1. Characterization of the Potential Energy Surface. We start by examining the topology of the adiabatic potential energy surfaces. A cut of the surfaces from the analytical model Hamiltonian is shown in Figure 4. It is taken at the lowest energy point of the conical intersection seam in the space of the Q_{14} and θ degrees of freedom, and the critical points are marked. The molecular geometry and energies at the critical points are also listed in Table 3, both from the model Hamiltonian and the quantum chemistry calculations. Despite the simplicity of the model, it is seen to reproduce the quantum chemistry very well. Of particular importance is the fact that the lowest point on the conical intersection seam, $\mathbf{Q}_{\mathrm{CoIn}}$, is correctly placed with respect to the Franck−Condon point, $\mathbf{Q}_{\mathrm{FC}}$. The two minima on the lower adiabatic surface, $\mathbf{Q}_{\tilde{\mathrm{X}}}$ are also in the right places, as is the transition point, $\mathbf{Q}_{\mathrm{TS}}$. Finally, the minimum on the upper surface, $\mathbf{Q}_{\tilde{\mathrm{A}}}$, is close to the minimum found in the quantum chemistry calculations. Discrepancies in the energies are of the order of 0.5 kcal mol^{-1}, except at the minima $\mathbf{Q}_{\tilde{\mathrm{X}}}$ where the difference is 1.6 kcal mol^{-1}.

$\mathbf{Q}_{\mathrm{FC}}$ is the equilibrium geometry of the neutral butatriene molecule. It is identical in both the model and quantum chemistry by construction. The force vector at this point, $\mathbf{F}_{\mathrm{FC}}$ in the dynamical coordinates defined in eq 15 is (0.0, −0.039, +0.046, +0.287, −0.135) in the model and (0.0, −0.032, −0.017, +0.292, +0.024) from the quantum chemistry. It is thus dominated by excitation of the ν_{14} vibration, and electronic excitation will result in vibrational motion occurring in the central C−C bond out of phase with vibration of the terminal C−C bond.

Moving to $\mathbf{Q}_{\mathrm{CoIn}}$, the central C−C bond has lengthened by 0.10 Å, and the terminal R_{CC1} bond length has shortened by 0.04 Å. The energies in Table 3 are taken relative to the vertical excitation energy from the neutral molecule vibronic ground state to the upper $\tilde{\mathrm{A}}$ state. Thus $\mathbf{Q}_{\mathrm{CoIn}}$ lies 2.5 kcal mol^{-1} below $\mathbf{Q}_{\mathrm{FC}}$, and as there is no barrier along the path between these points, passage to the intersection will be fast.

From eq 25 and the parameters in Table 1, the model Hamiltonian gradient difference vector, $\mathbf{F}_{\mathrm{GD}}$, in the dynamical coordinate system is (0.0, +0.006, +0.006, +0.502, −0.049), and effectively lies along the Q_{14} symmetric stretch normal mode. From eq 26, the derivative coupling vector, $\mathbf{F}_{\mathrm{DC}}$, lies parallel to the nonsymmetric normal mode Q_5 (the torsion angle), with a magnitude of 0.329. The quantum chemistry similarly calculates $\mathbf{F}_{\mathrm{GD}} = (0.0, +0.034, -0.036, +0.530, +0.017)$ and

TABLE 3: Position of Various Critical Points on the Adiabatic Potential Energy Surface from the $\tilde{X}^2B_{2g}$ and $\tilde{A}^2B_{2U}$ States of the Butatriene Radical Cation from CAS(5,6)/3-21G* Calculations and from a Model Hamiltonian Fitted To Reproduce the CAS Surfaces[a]

structure		R_{CC1} Å	R_{CC2} Å	R_{CH} Å	$\angle_{HCC}$ (deg)	θ (deg)	Q_{14}	energy kcal/mol
FC	model	1.329	1.262	1.073	117.61	0.0	0.00	0.076
	3-21G*	1.329	1.262	1.073	117.61	0.0	0.00	0.000
CoIn	model	1.281	1.362	1.091	120.40	0.0	−1.85	−2.287
	3-21G*	1.284	1.360	1.079	118.62	0.0	−1.82	−2.467
$\tilde{A}$	model	1.307	1.322	1.089	119.02	0.0	−1.04	−4.289
	3-21G*	1.304	1.323	1.077	120.59	0.0	−1.09	−3.756
$\tilde{X}$	model	1.351	1.250	1.085	119.04	31.01	0.42	−26.108
	3-21G*	1.346	1.248	1.074	119.12	32.17	0.35	−24.462
TS	model	1.307	1.322	1.089	119.02	0.0	0.79	−24.326
	3-21G*	1.358	1.237	1.073	119.15	0.0	0.66	−24.077
JT	3-21G*	1.329	1.262	1.073	117.61	90.0	−0.17	−7.220

[a] $\mathbf{Q}_{FC}$ is the Franck−Condon point, $\mathbf{Q}_{CoIn}$ is the lowest energy point on the D_{2h} conical intersection seam, $\mathbf{Q}_{\tilde{A}}$ is the energy minimum on the upper state, $\mathbf{Q}_{\tilde{X}}$ is the energy minima on the lower state, $\mathbf{Q}_{TS}$ is the transition state dividing the minima on the lower state, and $\mathbf{Q}_{JT}$ is the lowest energy point on the D_{2d} Jahn−Teller intersection seam (not present in model). Geometrical parameters are those in Figure 1, and Q_{14} is the (dimensionless normal mode) central C−C symmetric stretch shown in Figure 3. The zero point for the energy is taken at the Franck−Condon point, 244.896 kcal mol^{-1} (9.449 eV) above the neutral ground-state minimum.

$\mathbf{F}_{DC}$ lies along Q_5 with a value of 0.295. These vectors define the branching space, in which the degeneracy along the conical intersection seam is lifted. These two nuclear degrees of freedom dominate the dynamics, and in fact a two-mode model is able to reproduce the system dynamics well after suitable adjustments of the parameters to take into account the neglected modes in an average manner.[15]

The point $\mathbf{Q}_{CoIn}$ is clearly visible in Figure 4 as the point where the upper and lower adiabatic surfaces meet. Looking at the gradients of the two diabatic surfaces at this point, the model predicts that $\mathbf{F}^{(1)}_{CoIn} = (0.0, -0.009, -0.063, -0.719, +0.070)$ and $\mathbf{F}^{(2)}_{CoIn} = (0.0, -0.003, -0.056, -0.217, +0.021)$, whereas the quantum chemistry calculates $\mathbf{F}^{(1)}_{CoIn} = (0.0, -0.044, +0.048, -0.707, -0.022)$ and $\mathbf{F}^{(2)}_{CoIn} = (0.0, -0.011, +0.012, -0.176, -0.005)$. As the gradients on the two surfaces lie in the same direction, the intersection is classified as sloped.[31] In comparison to a peaked intersection, a sloped intersection means that classically the system is expected to recross the intersection before moving away on the lower surfaces. It also means that there is in a minimum on the upper adiabatic surface, $\mathbf{Q}_{\tilde{A}}$. This point lies between $\mathbf{Q}_{FC}$ and $\mathbf{Q}_{CoIn}$, with a depth in the region of 3.8 kcal mol^{-1} (quantum chemistry) and 4.3 kcal mol^{-1} (model) relative to that at $\mathbf{Q}_{FC}$.

Moving down onto the lower adiabatic surface, we note that it is periodic around the torsion angle. The minima, which lie symmetrically to either side of $\theta = 0°$ lower the symmetry of the stable geometry from D_{2h} to D_2, which is referred to as symmetry breaking due to the conical intersection. The minima on the lower surface lie a further 23.8 kcal mol^{-1} (model) or 22.0 kcal mol^{-1} (quantum chemistry) below the intersection. The wave packet will thus appear in the lower state with a large excess energy. The C−C bonds of the structures at these points, $\mathbf{Q}_{\tilde{X}}$, are close to those of $\mathbf{Q}_{FC}$, differing by less than 0.03 Å. The terminal CH_2 groups, however, have rotated relative to one another so that the dihedral angle $\theta \approx 32°$. Thus after passing through the intersection, torsional motion will begin. The minima are separated by a low transition state at $\mathbf{Q}_{TS}$ with $\theta = 0.0°$, and a barrier height of 1.8 kcal mol^{-1} (model) or 0.4 kcal mol^{-1} (quantum chemistry). The higher barrier in the model is due to the fact that the minima are deeper than in the quantum chemistry calculations.

From the quantum chemical calculations it is possible to look at the electronic origin of the conical intersection. In Figure 2 the set of p-functions incorporated in the CAS space is used to characterize the electronic configurations of the $\tilde{X}$ and $\tilde{A}$ states. In the lower state, an electron has been removed from the out-of-plane orbitals, whereas in the higher energy state it is removed from the in-plane orbitals. In a simple picture, both states have two double bonds, but the lower state has them across the central and one terminal C−C bond, whereas the upper state has them for the two terminal bonds. As a result, stretching the central C−C bond will destabilize the $\tilde{X}$ state, yet affecting the $\tilde{A}$ state very little. Thus stretching this bond will lead from the Franck−Condon point to a degeneracy. Compressing the terminal C−C bonds will stabilize both states. It is also clear from this simple picture as to why $\mathbf{F}_{FC}$ results in vibration of the central C−C bond.

There is one further critical point on the potential energy surfaces. When the CH_2 groups are rotated so that they are perpendicular to each other, the structure has D_{2d} symmetry. In this configuration, the neutral ground-state species has two unpaired electrons in degenerate orbitals composed of out-of-phase alternate carbon p-orbitals perpendicular to the molecular plane; i.e., one uses the p-orbitals from C_1 and C_3, and the other uses those from C_2 and C_4. It lies 32.5 kcal mol^{-1} in energy above the neutral ground-state D_{2h} structure. The first two states of the radical cation remove these two electrons, and are thus degenerate. From the symmetry of the molecule here, it is an $E \otimes \beta$ Jahn−Teller intersection, and the degeneracy can be removed by vibrations with B_1 and B_2 symmetry. The derivative coupling vector is again provided by the torsion angle, which now has B_1 symmetry. The gradient difference is an antisymmetric vibration along the carbon chain, with the central two carbon atoms moving together relative to the terminal carbon atoms.

The geometry of the lowest energy point on the degenerate seam, labeled $\mathbf{Q}_{JT}$, is also listed in Table 3. This second seam of intersection between the two states is not linked to that at the D_{2h} geometry explored above. The two intersection seams are in fact separated on the upper surface by a significant barrier. The Jahn−Teller seam, however, lies 4.8 kcal mol^{-1} below the D_{2h} conical intersection, and is thus energetically accessible after crossing to the lower surface.

Unfortunately, this Jahn−Teller seam is not present in the model. This is partly due to the reduced coordinate set used; the antisymmetric stretch that provides the gradient difference is not included. More importantly, in the set of coordinates used, the seam should be present as a crossing seam, and due to the model adopted this is not the case. The lower surface fits that of the quantum chemistry, but the upper surface does not meet

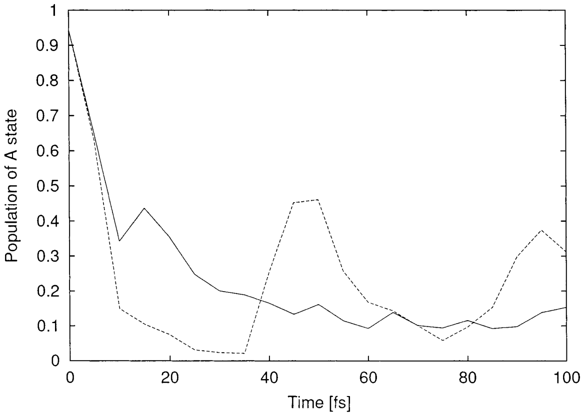

Figure 5. Population of the upper, $\tilde{A}^2B_{2u}$, adiabatic state of the butatriene radical cation after the removal of an electron from the neutral ground state. Full line: results from 80 direct dynamics trajectories with surface hopping. The initial population of 0.84 is the magnitude of the adiabatic component in the initial diabatic wave packet. Dashed line: results from wave packet dynamics on a five-mode model.

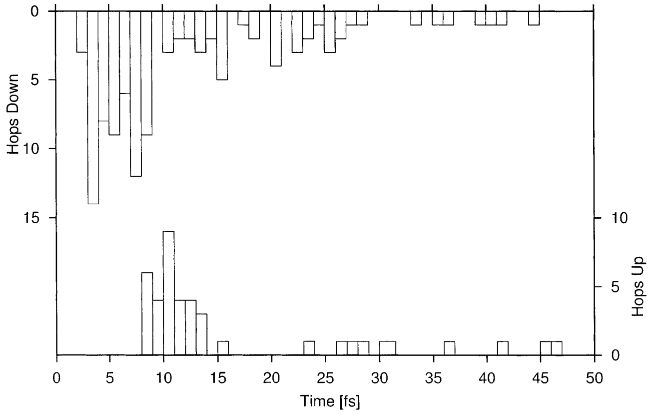

Figure 6. Total number of hops between states in a set of 80 trajectories over the coupled potential energy surface of the $\tilde{X}^2B_{2g}/\tilde{A}^2B_{2u}$ states of the butatriene radical cation as a function of time. The hops are collected in 1 fs bins. The upper boxes show the hops down from the upper state (left-hand axis), and the lower boxes the hops up from the lower state (right-hand axis).

here; the periodicity of the coupling does not allow this. As will be seen, however, this region of space is hardly touched by the evolving wave packet and this region plays a minor role in the dynamics, negligible at short times.

3.2. Molecular Dynamics through the Intersection. For the direct dynamics calculations, 80 trajectories were generated, using points sampled on the neutral ground-state for the initial conditions and starting the propagation on the $\tilde{A}$ state. Each trajectory was propagated for 100 fs and took about 10 h on an IBM SP2 machine.

Figure 5 shows the rate of population transfer between the adiabatic states after the excitation. Values were calculated every 5 fs. The population at time $t = 0$ is not 1.0 as the excitation (electron removal) was taken as a diabatic process, and so the $\tilde{X}$ adiabatic state is also populated directly to a small extent. The direct dynamics results have been normalized to match the quantum dynamics adiabatic $\tilde{A}$ population at $t = 0$. The transfer is obviously very fast, which is due to the fact that the conical intersection lies close to the Franck−Condon point and is reached almost immediately after excitation. The efficiency of the transfer is such that after 20 fs the wave packet calculations (dashed line) indicate that less than 10% is left in the upper state. Recurrences are then seen at 50 and 100 fs, where an appreciable recrossing to the upper state takes place. Such recurrences are due to the coherent nature of the interstate crossing. As will be seen in more detail later, the quantum wave packet is not immediately dispersed throughout phase space after going through the intersection, but periodically regroups back in the crossing region. Eventually, this coherence will be lost, and the recurrences die out.

The surface hopping of the direct dynamics calculations also show that the transfer is extremely fast, and the initial rate of transfer matches the quantum calculations very well. Population in this case is simply the percentage of trajectories associated with a particular state, and so over half the trajectories undergo a hop to the lower state within 10 fs. A small recrossing then occurs due to hopping between the states while the trajectories are still in the crossing region, before the population of the upper state stabilizes at around 15%. No significant recurrence is seen at 50 or 100 fs. The behavior of the semiclassical trajectories is reflected in the number of hops per unit time in both directions, shown in Figure 6. Hopping down starts after 2 fs, and hopping up after 8 fs. After 30 fs the transfer is effectively finished and the trajectories have moved away from the crossing region. After this only occasional hops occur when a trajectory finds its way back to the intersection.

On examining the trajectories, a number of distinct patterns are seen to occur. Examples are shown in Figure 7. The trajectories are plotted here in the space of the θ and Q_{14} coordinates as a single line with the starting point at the black triangle. The plot thus shows the configurations covered in this space, which is related to the derivative coupling and gradient difference vectors. In addition, information is given on the electronic state occupied during the time evolution. When the system is in the upper electronic adiabatic state, the trajectory is a dashed line, whereas when it has switched to the lower state the trajectory is a full line. As the majority of the time is spent in the lower adiabatic state, the lower potential energy surface is shown as a contour plot. Full circles, ●, show where a hop down occurs, and open circles, ○, denote a hop up. For example, (a) shows a trajectory that starts close to the Franck−Condon point at (0, 0). It evolves initially on the upper surface along Q_{14} in a negative direction until a hop down onto the lower surface occurs at the black circle. This point is close to the conical intersection, which lies at the point $(\theta, Q_{14}) = (0.0, -1.9)$. After this time, the trajectory explores the double minima of the lower surface.

All the trajectories approach the crossing region within a few femtoseconds. Of the 80 trajectories, 39 cross to the lower state directly with a single hop and then explore the lower surface, as shown in (a). In a different class, 30 trajectories undergo a double hop while traversing the crossing region, shown in (c). This is due to the sloped nature of the intersection, so that the trajectory crosses to the lower surface and then travels up the repulsive wall. This forces it to return to the crossing region where it crosses back to the upper state. After a short time it then returns to the lower state and moves away from the intersection. Five trajectories undergo multiple crossings while in this region, and an example of this is shown in Figure 7d. Finally, six trajectories do not cross at all, and remain trapped on the upper surface.

After crossing to the lower state, the trajectories explore the minima. In eight cases after a number of vibrations on the lower surface, the trajectory finds its way back to the intersection and crosses back up, and then down again. This is exemplified in Figure 7b. Five further trajectories also cross back to the upper surface after a long excursion on the lower one, but do this via the D_{2d} Jahn−Teller intersection at $\theta = 90°$. An example of

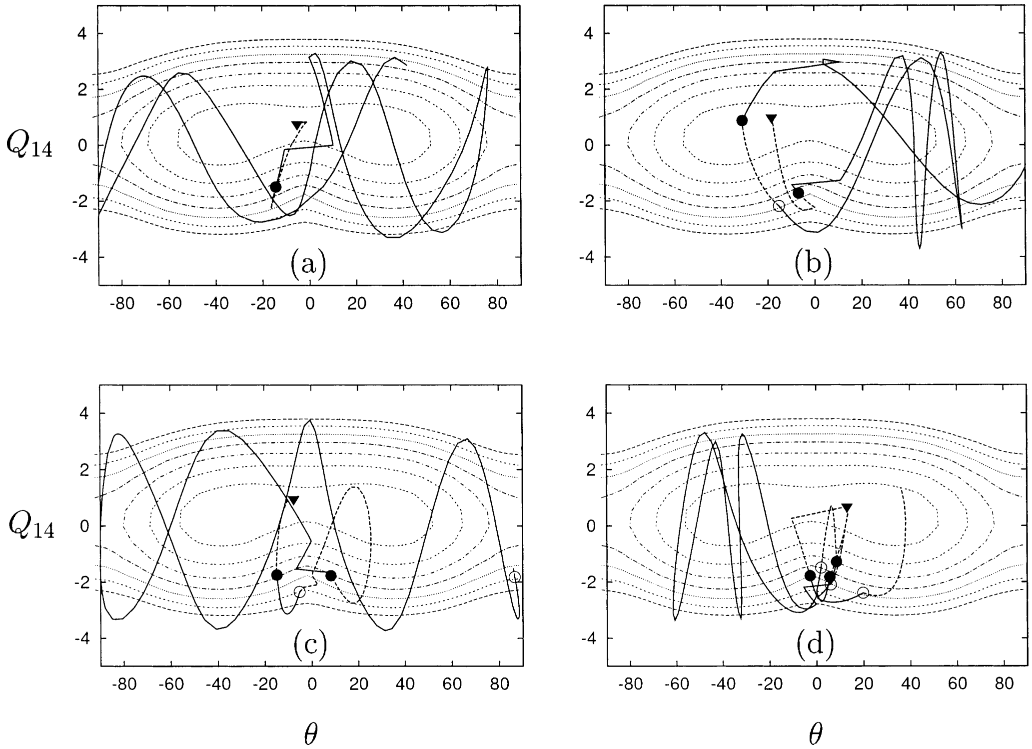

Figure 7. Example trajectories demonstrating the possible evolution of the butatriene radical cation after formation in the $\tilde{A}^2B_{2u}$ state. (a) Direct interstate crossing followed by exploration of the lower surface. (b) Interstate crossing with a recrossing occurring after exploration of the lower surface. (c) Double crossing before exploration of the lower surface. (d) Multiple crossings. The trajectories are plotted in the space of the θ and Q_{14} coordinates, and the lower adiabatic potential energy surface is shown in each case as a contour plot. The ▼ shows the start point. Full circles ● show where a hop down occurs, and open circles ○ denote a hop up. A dashed section of trajectory is where it is running on the upper surface.

this can be seen at the end of the trajectory shown in (c). This is an indication that this second intersection seam may indeed be important for the system dynamics at longer times.

The time evolution of the three significant geometrical parameters of the molecule are plotted in Figure 8. The values from the direct dynamics calculations are averages over the 80 trajectories. For the quantum dynamics, the results are expectation values of the density along the appropriate coordinates. For the torsion angle, the value is calculated over the range $0 \rightarrow \pi$. In general, the semiclassical trajectories show good agreement with the quantum dynamics results, especially over the first 50 fs.

As expected from the analysis of the potential energy surface above, initial motion is along the normal mode vector for the ν_{14} vibration, i.e., extension of the central C−C bond and compression of the terminal C−C bond. This motion occurs with a period of approximately 15 fs, which corresponds to the ground-state period of this vibration. The average value of the torsion angle starts to change after approximately 5 fs. Excitation of this mode is related to passing through the intersection, and thus this delay is due to the time taken for the wave packet to reach the intersection.

For the model Hamiltonian, a time period for the torsional motion can be estimated from the leading term in the diabatic potential, eq 13. Thus

$$\frac{\omega_\theta}{2} \approx \frac{\sum_n A_n n^2}{(r_0\sqrt{\omega_5 m_H})^2} \qquad (30)$$

Using $r_0\sqrt{\omega_5 m_H} = 4.35$ au, this gives a frequency of approximately 756 cm^{-1}, or a period of 42 fs. This clearly matches the periodicity seen in the quantum dynamics calculations. The semiclassical calculations appear to have a slightly longer period for this motion of approximately 55 fs. Much larger motion is also seen in this degree of freedom in the trajectory calculations.

For a more detailed comparison of the molecular dynamics, we will now look at the snapshots of the evolving wave packet. Figure 9 shows the results from the quantum dynamics calculations, showing the wave packet as it traverses the conical intersection as a series of snapshots. The adiabatic density is plotted in the space of the θ and Q_{14} modes, integrating over the remaining degrees of freedom:

$$\rho(\theta,Q_{14}) = \int_{-\infty}^{\infty} dQ_8\, dQ_{12}\, dQ_{15}\, \Psi\Psi^* \qquad (31)$$

The two columns show the density for the two states. The upper panel in each column shows the potential energy surface. At $t = 0$, the density is mostly on the upper surface, but as mentioned above, the lower surface is also lightly populated. Note that for reasons of scale the top of the packet is cut off. As time progresses, the wave packet moves across the upper surface, driven by the forces on the nuclei due to the creation of the nonstationary wave packet by the excitation process. Due to the conical intersection, transfer of population starts immediately, and, as seen in the populations in Figure 5, this is almost complete after 10 fs.

As the population vanishes from the upper state, it appears in the lower state emerging from the region of the conical intersection. The wave packet has a definite directionality to it, and moves around the intersection into the two minima. The motion after 10 fs sees the wave packet on the lower surface split into two parts and spread out. By 40 fs the wave packet is moving back together at the intersection. This is the start of the recurrence.

To compare this with the picture from the direct dynamics, the wave packet dynamics is shown again in Figure 10. This

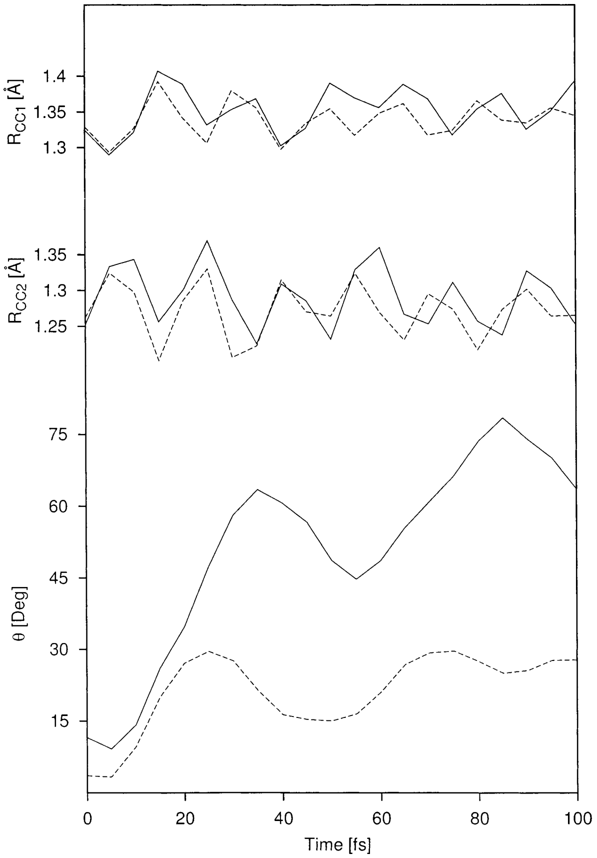

Figure 8. Time evolution of the geometrical parameters of the butatriene radical cation after formation in the $\tilde{A}^2B_{2u}$ state. Upper panel: terminal C−C bond. Middle panel: central C−C bond. Lower panel: dihedral angle. Full lines are the average value from a set of 80 trajectory surface hopping direct dynamics calculations. Dashed lines are expectation values from wave packet dynamics calculations, with the dihedral taken in the range 0−180°.

time, the trajectories of the direct dynamics calculations are shown as crosses superimposed on the wave packet contours, which correspond to the picture in Figure 9. At the start, a dense cluster of points indicate that the direct dynamics is sampling the space in the region of the initial wave packet. The initial motion follows the wave packet and hops to the lower surface take place in the region of the intersection, which lies at (θ, Q_{14}) = (0.0, − 1.9). The direct dynamics thus simulate the wave packet reasonably well in the time scale of the transfer. The dynamics after transfer are, however, different. The quantum wave packet moves diagonally away from the intersection, before dividing into two parts in the two minima. In contrast, after crossing to the lower surface, the trajectories spread out, and after 40 fs are seen to cover the whole region and do not regroup.

4. Conclusions

We are presently at the start of investigating the use of direct dynamics in the study of nonadiabatic processes, and the aim of this study was to see how well simple direct dynamics calculations perform for the description of a realistic process. The system chosen, the removal of an electron from butatriene is an ideal test case as the topology of the surfaces is such that population transfer after excitation to the upper state starts immediately. At the level of theory used, CASSCF/3-21G*, state-of-art direct dynamics as implemented in the GAUSSIAN program are not prohibitively expensive for this molecule. As a result, it is possible to run a number of trajectories, which is necessary for a comparison with accurate quantum dynamics calculations.

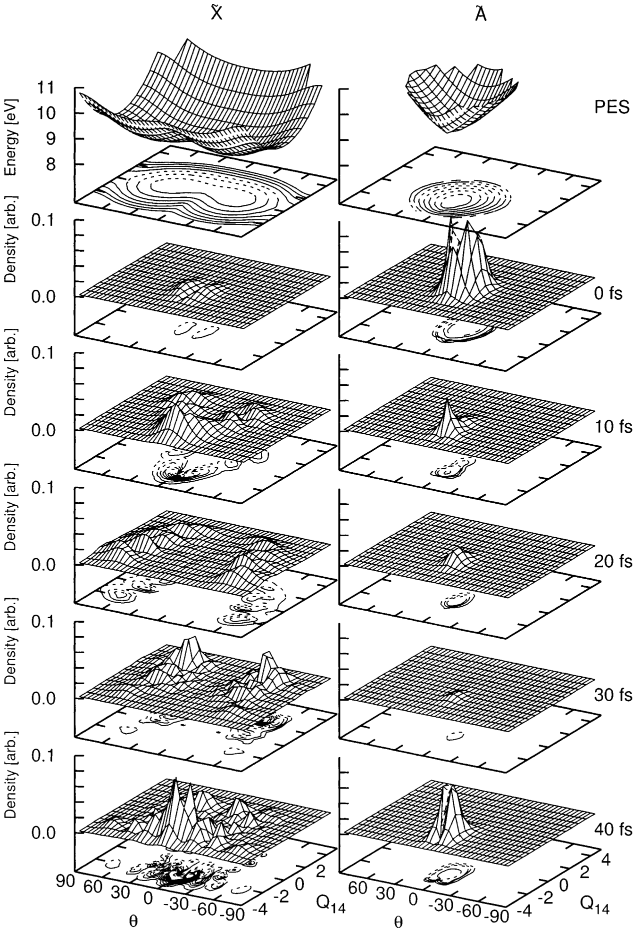

Figure 9. Wave packet dynamics of the butatriene radical cation after its production in the Ã state, shown as snapshots of the adiabatic density (wave packet amplitude squared) at various times in the space of the θ and Q_{14} coordinates. The right-hand plots relate to the Ã, and left-hand plots the X̃ adiabatic states. The top panels shows the adiabatic potential energy surfaces. Remaining panels show the density at various times. The initial structure represents the neutral ground state vibronic wave function vertically excited onto the diabatic Ã state.

The results presented here show that the direct dynamics trajectories using surface hopping are qualitatively in agreement with the results of wave packet propagation calculations. The time scale for population transfer is similar, and the final populations also reasonable. There is a difference, however, in the pattern of the recurrences, when population is transferred back to the upper state. In the semiclassical calculations, the sloped nature of the intersection means that trajectories recross the intersection region immediately after hopping down. In contrast, the quantum dynamics calculations show recrossings at regular 50 fs intervals.

One of the strengths of the method is that the assumptions usually made in the models used for studying the dynamics of large molecules, such as ignoring certain modes or choosing a pre-defined form for the potentials, are not made here. In the model used here, for example, only five degrees of freedom are included. This Hamiltonian is complete to first-order vibronic coupling and is good for the description of the dynamics during the initial crossing of the conical intersection. It may, however, be less accurate for the dynamics at longer times (over 100 fs). In particular, dephasing of the wave packet will be suppressed. In the full system, energy will be transferred slowly to the

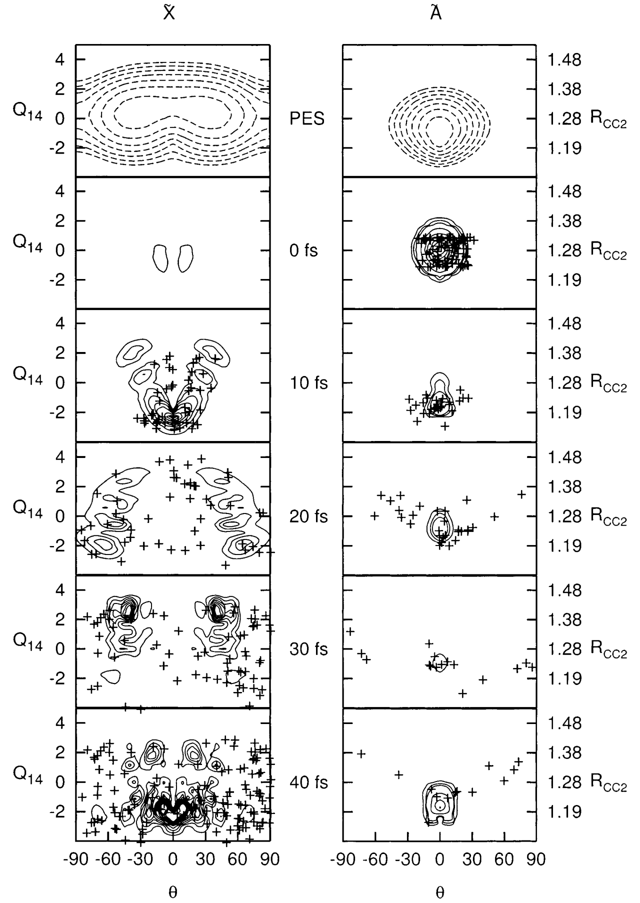

Figure 10. Molecular dynamics of the butatriene radical cation after its production in the Ã state, shown as snapshots of the adiabatic density at various times in the space of the θ and Q_{14} coordinates. The right-hand axis gives the central C−C bond length, in Å, corresponding to the Q_{14} coordinate. The top panels shows the adiabatic potential energy surfaces as contour plots. Remaining panels show the density at various times. The contours plot the results from wave packet calculations (see Figure 9), and the crosses are the points on the trajectories from the direct dynamics.

degrees of freedom ignored here. This will result in the wave packet spreading out more than the five-mode model will allow. The recurrences seen would thus be reduced in intensity, and die out quicker if all the degrees of freedom were included. The basic features of the quantum dynamics would, however, not be altered if all modes were included.

Another factor missed in the model, which may affect the long-time behavior of the system, is that the potentials are not fitted to reproduce the Jahn−Teller intersection at the perpendicular D_{2d} geometry. If this seam is important for the dynamics of the system, the quantum dynamics calculations will completely miss this effect. The direct dynamics of course will let the system cross at this seam if it finds it, and the calculations indeed indicate that the system is finding its way to this seam at later times.

The comparison of the time evolution of the densities, however, indicate that the direct dynamics do not reproduce the details of the quantum dynamics during the initial crossing through the conical intersection. In particular, the trajectories do not move away from the intersection on the ground state in the same manner. This may be due to differences in the surfaces used in the two calculations leading to different dynamics. It is, however, more likely to be a consequence of the lack of nuclear coherence during the nonadiabatic process: the semiclassical trajectories arrive on the lower surface in a manner uninfluenced by each other. In future work we intend to address this problem by the use of more sophisticated direct dynamics, probably using a Gaussian wave packet based method to include some quantum character into the nuclear dynamics.

References and Notes

(1) Chen, W.; Hase, W. L.; Schlegel, H. B. *Chem. Phys. Lett.* **1994**, *228*, 436−442.

(2) Worth, G. A.; Robb, M. A. *Adv. Chem. Phys.* **2002**, *124*, 355−432.

(3) Tully, J. C.; Preston, R. K. *J. Chem. Phys.* **1971**, *55*, 562−572.

(4) Ben-Nun, M.; Quenneville, J.; Martínez, T. J. *J. Phys. Chem. A* **2000**, *104*, 5162−5175.

(5) Ben-Nun, M.; Martínez, T. J. *Chem. Phys. Lett.* **1998**, *298*, 57−65.

(6) Vreven, T.; Bernardi, F.; Garavelli, M.; Olivucci, M.; Robb, M. A.; Schlegel, H. B. *J. Am. Chem. Soc.* **1997**, *119*, 12687−12688.

(7) Sanchez-Galvez, A.; Hunt, P.; Robb, M. A.; Olivucci, M.; Vreven, T.; Schlegel, H. B. *J. Am. Chem. Soc.* **2000**, *122*, 2911−2924.

(8) Smith, B. R.; Bearpark, M. J.; Robb, M. A.; Bernardi, F.; Olivucci, M. *Chem. Phys. Lett.* **1995**, *242*, 27−32.

(9) Bearpark, M. J.; Bernardi, F.; Clifford, S.; Olivucci, M.; Robb, M. A.; Smith, B. R.; Vreven, T. *J. Am. Chem. Soc.* **1996**, *118*, 169−175.

(10) Bearpark, M. J.; Bernardi, F.; Olivucci, M.; Robb, M. A.; Smith, B. R. *J. Am. Chem. Soc.* **1996**, *118*, 5254−5260.

(11) Deumal, M.; Bearpark, M. J.; Smith, B. R.; Olivucci, M.; Bernardi, F.; Robb, M. A. *J. Org. Chem.* **1998**, *63*, 4594−4600.

(12) Garavelli, M.; Smith, B. R.; Bearpark, M. J.; Bernardi, F.; Olivucci, M.; Robb, M. A. *J. Am. Chem. Soc.* **2000**, *122*, 5568−5581.

(13) Brogli, F.; Heilbronner, E.; Kloster-Jensen, E.; Schmelzer, A.; Manocha, A. S.; Pople, J. A.; Radom, L. *Chem. Phys.* **1974**, *4*, 107−119.

(14) Cederbaum, L. S.; Domcke, W.; Köppel, H.; von Niessen, W. *Chem. Phys.* **1977**, *26*, 169.

(15) Köppel, H.; Domcke, W.; Cederbaum, L. S. *Adv. Chem. Phys.* **1984**, *57*, 59.

(16) Cattarius, C.; Worth, G. A.; Meyer, H.-D.; Cederbaum, L. S. *J. Chem. Phys.* **2001**, *115*, 2088−2100.

(17) Frisch, M. J.; Trucks, G. W.; Schlegel, H. B.; Scuseria, G. E.; Robb, M. A.; Cheeseman, J. R.; Zakrzewski, V. G.; Montgomery, J. A., Jr.; Stratmann, R. E.; Burant, J. C.; Dapprich, S.; Millam, J. M.; Daniels, A. D.; Kudin, K. N.; Strain, M. C.; Farkas, O.; Tomasi, J.; Barone, V.; Mennucci, B.; Cossi, M.; Adamo, C.; Jaramillo, J.; Cammi, R.; Pomelli, C.; Ochterski, J.; Petersson, G. A.; Ayala, P. Y.; Morokuma, K.; Malick, D. K.; Rabuck, A. D.; Raghavachari, K.; Foresman, J. B.; Ortiz, J. V.; Cui, Q.; Baboul, A. G.; Clifford, S.; Cioslowski, J.; Stefanov, B. B.; Liu, G.; Liashenko, A.; Piskorz, P.; Komaromi, I.; Gomperts, R.; Martin, R. L.; Fox, D. J.; Keith, T.; Al-Laham, M. A.; Peng, C. Y.; Nanayakkara, A.; Challacombe, M.; Gill, P. M. W.; Johnson, B.; Chen, W.; Wong, M. W.; Andres, J. L.: Gonzalez, C.; Head-Gordon, M.; Replogle, E. S.; Pople, J. A. *Gaussian 99*, Development Version, revision C.01; Gaussian, Inc.: Pittsburgh, PA, 2000.

(18) Boys, S. F. *Rev. Mod. Phys.* **1960**, *32*, 300.

(19) Chapman, S.; Bunker, P. *J. Chem. Phys.* **1975**, *62*, 2890−2899.

(20) Sloane, C. S.; Hase, W. L. *J. Chem. Phys.* **1977**, *66*, 1523−1533.

(21) Hillery, M.; O'Connell, R. F.; Scully, M. O.; Wigner, E. P. *Phys. Rep.* **1984**, *106*, 122−167.

(22) Helgaker, T.; Uggerud, E.; Jensen, H. J. A. *Chem. Phys. Lett.* **1990**, *173*, 145−150.

(23) Klein, S.; Bearpark, M. J.; Smith, B. R.; Robb, M. A.; Olivucci, M.; Bernardi, F. *Chem. Phys. Lett.* **1998**, *292*, 259−266.

(24) Tully, J. C. *J. Chem. Phys.* **1990**, *93*, 1061.

(25) Ragazos, I. N.; Robb, M. A.; Bernardi, F.; Olivucci, M. *Chem. Phys. Lett.* **1992**, *197*, 217.

(26) Bearpark, M. J.; Robb, M. A.; Schlegel, H. B. *Chem. Phys. Lett.* **1994**, *223*, 269.

(27) Robb, M. A.; Garavelli, M.; Olivucci, M.; Bernardi, F. In *Reviews in Computational Chemistry*; Lipkowitz, K., Boyd, D., Eds.; John Wiley and sons: New York, 2000; Vol. 15, pp 87−146.

(28) Meyer, H.-D.; Manthe, U.; Cederbaum, L. S. *Chem. Phys. Lett.* **1990**, *165*, 73.

(29) Manthe, U.; Meyer, H.-D.; Cederbaum, L. S. *J. Chem. Phys.* **1992**, *97*, 9062.

(30) Beck, M. H.; Jäckle, A.; Worth, G. A.; Meyer, H.-D. *Phys. Rep.* **2000**, *324*, 1−105.

(31) Atchity, G. J.; Xantheas, S. S.; Ruendenberg, K. *J. Chem. Phys.* **1991**, *95*, 1862−1876.

(32) Worth, G. A.; Beck, M. H.; Jäckle, A.; Meyer, H.-D. *The MCTDH Package*, Version 8.2; University of Heidelberg: Germany, 2000. See http://www.pci.uni-heidelberg.de/tc/usr/mctdh/